sustainability

MDPI

Article

Eco-Friendly Photocatalytic Treatment of Dyes with Ag Nanoparticles Obtained through Sustainable Process Involving *Spirulina platensis*

Agnieszka Sidorowicz [1], Giacomo Fais [1,2], Francesco Desogus [1,2,*], Francesco Loy [3], Roberta Licheri [1,2], Nicola Lai [1,2], Giacomo Cao [1,2,4] and Alessandro Concas [1,2,*]

[1] Interdepartmental Centre of Environmental Science and Engineering (CINSA), University of Cagliari, Via San Giorgio 12, 09124 Cagliari, Italy; a.sidorowicz@studenti.unica.it (A.S.); giacomo.fais@unica.it (G.F.); roberta.licheri@unica.it (R.L.); nicola.lai@unica.it (N.L.); giacomo.cao@unica.it (G.C.)
[2] Department of Mechanical, Chemical and Materials Engineering, University of Cagliari, Via Marengo 2, 09123 Cagliari, Italy
[3] Department of Biomedical Sciences, University of Cagliari, Cittadella Universitaria, SS 554, Km 4.5, 09042 Monserrato, Italy; floy@unica.it
[4] Center for Advanced Studies, Research and Development in Sardinia (CRS4), Loc. Piscina Manna, Building 1, 09050 Pula, Italy
* Correspondence: francesco.desogus2@unica.it (F.D.); alessandro.concas@unica.it (A.C.)

Abstract: The development of efficient photocatalysts is crucial in addressing water pollution concerns, specifically in the removal of organic dyes from wastewater. In this context, the use of silver nanoparticles (Ag NPs) might represent a method to achieve high dye degradation efficiencies. On the other hand, the classical Ag NP production process involves several reactants and operating conditions, which make it poorly sustainable. In the present work, Ag NPs were synthesized according to a new sustainable process involving the use of natural extracts of *Spirulina platensis* and milder operating conditions. The material was also calcined to determine the influence of organic content on the properties of Ag NPs. The X-ray diffraction (XRD) analysis displayed the AgCl and Ag phases with a crystalline size of 11.79 nm before calcination. After calcination, only the Ag phase was present with an increased crystalline size of 24.60 nm. Fourier Transform Infrared Spectroscopy (FTIR) confirmed the capping role of the metabolites from the extract. Scanning Electron Microscopy (SEM) and Transmission Electron Microscopy (TEM) revealed the spherical or quasi-spherical morphologies with agglomeration due to the calcination. Energy-dispersive X-ray spectroscopy (EDX) and Thermogravimetric (TGA) analyses further confirmed the involvement of metabolites in the synthesis of Ag NPs. The optical changes in the products were observed in a UV-Vis analysis. The Ag NPs were tested for their photocatalytic activity against the laboratory dye brilliant blue r in visible light in various conditions. The highest degradation efficiency of 81.9%, with a k_{app} value of 0.00595 min^{-1}, was observed in alkaline medium after 90 min of light irradiation.

Keywords: *Spirulina platensis*; sustainable production of silver nanoparticles; photocatalytic degradation; advanced oxidation process; sustainable chemistry

Citation: Sidorowicz, A.; Fais, G.; Desogus, F.; Loy, F.; Licheri, R.; Lai, N.; Cao, G.; Concas, A. Eco-Friendly Photocatalytic Treatment of Dyes with Ag Nanoparticles Obtained through Sustainable Process Involving *Spirulina platensis*. *Sustainability* **2024**, *16*, 8758. https://doi.org/10.3390/su16208758

Academic Editor: Kaan Kalkan

Received: 9 July 2024
Revised: 13 September 2024
Accepted: 8 October 2024
Published: 10 October 2024

1. Introduction

While industrialization has improved standards of living, it has also had a negative impact on the environment by producing hazardous chemical species. The produced contaminants are mostly organic dyes, which are waste products of the tanneries, paint, and textile industries [1]. Subsequently, their discharge into water bodies without proper treatment can be a major source of water pollution. Due to their complex aromatic structure, they can maintain toxicity and stability over a prolonged time, ultimately damaging aquatic

life and human health [2]. Their engineered ability to resist degradation hinders biodegradability [3]; therefore, the research focuses on the development of various techniques to combat this issue.

One of the most efficient methods used for wastewater treatment is the advanced oxidation process (AOP), such as photocatalysis. The mechanism behind it relies on the absorption of light energy higher than the bandgap energy of the catalyst, which results in the excitation of the electron in the valence band to the conduction band, leaving behind the holes [4]. The electron–hole pairs participate in redox reactions generating reactive oxygen species (ROS), such as hydroxyl radicals, which oxidize the dye into lower-molecular-weight products [5]. The efficiency of the process relies on the properties of the used catalyst, such as the bandgap energy or electron transfer [6–8]; thus, various synthesis techniques were studied to obtain highly valuable products.

Considering many synthesis routes, the biological approach has emerged as an alternative way to decrease high operating costs and the generation of toxic by-products [9]. Various organisms have been utilized due to the abundance of metabolites in their structure that can act as reducing and stabilizing agents during the synthesis of nanoparticles [9]. Recently, microalgae, typically studied for their nutritional value, are gaining more attention also as a source of metabolites that can participate in the synthesis of nanoparticles [10,11]. Other advantages of microalgae include rapid growth and ease of cultivation, which make them useful for a wide range of applications [12–14].

Among many microalgae, *Spirulina platensis* has a significantly increased protein content besides a high concentration of vitamins, essential fatty acids, and minerals [15]. The *S. platensis* biomass has been utilized in the past for the synthesis of silver nanoparticles (Ag NPs) tested against malachite green biosorption from wastewater [16]. Moreover, the Ag NP photocatalytic activity was studied against methylene blue and eosin y, showing excellent dye degradation properties [17,18]. However, to the best of our knowledge, Ag NPs synthesized using *S. platensis* have not been studied for the degradation of brilliant blue r (BBR), a common laboratory dye used mainly for protein staining.

In the current work, the methanolic extract from *S. platensis* was utilized for the synthesis of Ag NPs. The product was also calcined to determine the influence of organic capping agents on the structure and activity. The material was characterized and applied for the photocatalytic degradation of BBR in the varying parameters of the light intensity, dye concentration, catalyst concentration, pH, or presence or absence of organic content. The photocatalytic mechanism was studied to develop a better understanding of the degradation pathway, which might aid in the optimization of the conditions for the removal of hazardous BBR dye from the environment.

2. Materials and Methods

2.1. Preparation of Photocatalyst

The *Spirulina platensis* (courtesy of TOLO Green, Arborea, Italy) was cultivated in modified Zarrouk Medium. The medium was prepared according to the previously reported composition [11], and K_2SO_4 and $MgSO_4$ were added aseptically after setting the pH to 9 and autoclaving. The culture was cultivated under continuous illumination of 58 W fluorescent lamps (Osram®, Milan, Italy) with a photon flux of 30 µmol/m^2/s^1 and 250 RPM stirring for 30 days to obtain a suitable amount of biomass. Then, it was centrifuged at 1500 RPM at 4 °C (Heraeus® Megafuge® 1.0R, Milan, Italy) and the algal biomass was dried at room temperature.

In the next step, 4.3 g of dried residue was combined with 260 mL of methanol (Merck® LiChrosolv® hypergrade, Milan, Italy). The flask was sonicated for 30 min (Soltec® Sonica® 2400 ETH S3, Milan, Italy) and stirred at 250 RPM (IKA® RH Digital Magnetic Stirrer, Milan, Italy) for the next 30 min to release the cell content into the solvent. In order to remove the cell debris, the suspension was filtered using standard 11 µm filtration paper (Whatman®, Milan, Italy) and then evaporated using a rotary evaporator (BUCHI Rotavapor™ R-210 Rotary Evaporator System, Milan, Italy) to remove about 70% of the

methanol. The concentrated extract was then diluted with MiliQ H_2O (Millipore®, Milan, Italy) to the final volume of 520 mL and used for the synthesis of the nanoparticles.

The flask containing *S. platensis* extract was heated to 85 °C and stirred at 250 RPM (IKA® RH Digital Magnetic Stirrer, Milan, Italy). Then, 0.1 M of silver nitrate (Carlo Erba®, Milan, Italy) was added, and after 15 min, the pH was raised to 8 by using 1.25 M NaOH. From the moment of adding the salt, the reaction continued for 1.5 h and then it was left for maturation at room temperature. Subsequently, the liquid was centrifuged at 4000 RPM at 8 °C (Heraeus® Megafuge® 1.0R, Milan, Italy) and the residue was repeatedly washed with MiliQ H_2O (Millipore®, Milan, Italy) in the two washing cycles. Then, the residue was dried at 80 °C for 24 h, ground using a mortar and pestle, and divided into two parts. One part was stored in an Eppendorf tube in the absence of light and the other was calcined in a muffle furnace (Gelman Instrument®, Chelsea, UK) for 2 h at 600 °C. After calcination, the samples were stored in the same conditions as the samples before calcination.

2.2. Characterization

The X-ray diffraction (XRD) analysis of the Ag NPs was performed using an X-ray Diffractometer (Phillips®, PW1830/00, Amsterdam, The Netherlands and D8 Advance, Bruker AXS®, Milan, Italy). The scanning was conducted with a diffraction angle between 12° and 90° at 0.1° per 10 s, at 40 kV and 30 mA, using CuKα (λ = 1.54 Å) radiation. Phase identification was obtained by using Diffrac.Eva software v.6.1.0.4 according to the COD database. The crystallite size was calculated after baseline correction using Scherrer's formula and the Williamson and Hall method to evaluate both the crystallite size and microstrain. Additionally, the lattice parameters were estimated from XRD data [19].

The functional groups present on the Ag NPs were analyzed using Fourier Transform Infrared Spectroscopy (FT/IR-6700, Jasco, Tokyo, Japan) in the range 500–4000 cm^{-1}.

A Scanning Electron Microscopy (SEM) analysis was conducted using a Hitachi S4000 FEG HRSEM (Hitachi Ltd., Tokyo, Japan) operated at 20 kV with image acquisition software Quartz PCI Version 8.0 (Quartz Imaging Corporation, Vancouver, BC, Canada). Before the analysis, the samples were coated with 2 nm of platinum to enhance the contrast. An EDX analysis was obtained using an UltraDry EDX Detector (Thermo Fisher Scientific®, Madison, WI, USA) and NSS3 software Version 3 (Thermo Fisher Scientific®, Madison, WI, USA). A Transmission Electron Microscopy (TEM) analysis was conducted using a JEOL JEM 1400 Plus TEM with an EDX probe "X-Max 80T" (Oxford Instruments, Abingdon, UK) at CeSAR core facilities with an accelerating voltage of 100 kV.

The thermal properties were examined by Thermogravimetric Analysis (TGA) using a Differential Thermal Analyzer TG/DSC (NETZSCH® STA 409 PC, Verona, Italy) in a heating range of 25–1000 °C at 10 °C/min with airflow of 100 mL/min.

UV-Vis absorption measurements were carried out using a CARY 50 spectrophotometer (Varian Inc., Palo Alto, CA, USA) with a cell path length of 10 mm. The UV-Vis spectra of the Ag NPs were recorded in the wavelength range of 200–750 nm. The direct bandgap energy was calculated from the Tauc relation (Equation (1)):

$$(\alpha h\nu)^2 = (h\nu - E_g), \quad (1)$$

where α is the molar extinction coefficient, *h* is the Plank's constant, ν is the light frequency, and Eg is the bandgap energy. The bandgap energy was calculated by linear fit extrapolation of the plot of $(\alpha h\nu)^2$ against energy.

2.3. In Situ Photocatalysis

First, the calibration line was obtained by assessing the correlation between the absorbance and concentration of the dye (S1). Before each photocatalytic experiment, 50 mL of ddH_2O was mixed with Ag NPs and sonicated for 15 min in a sonication bath (Soltec® Sonica® 2400 ETH S3, Milan, Italy) to ensure even dispersion. Firstly, the baseline of the solution of dispersed Ag NPs was generated. Then, the reaction sample was mixed with various concentrations of BBR (Sigma-Aldrich®, Milan, Italy) dye in ethanol (500 mg/L).

The flask was constantly slowly stirred for 30 min in the dark to ensure that equilibrium was reached. Next, the solution was irradiated by a warm white 10.5 W LED bulb (Phillips, Milan, Italy), and the irradiation intensity was monitored by a luxmeter (HD2302.0 Delta-Ohm, Padua, Italy). The emission spectrum as provided by the manufacturer is shown in Figure 1. The peristaltic pump (Keenso DC, Shenzhen, China) was used to circulate the liquid between the flask and a 10 mm flow-through cuvette attached to the UV-VIS Spectrophotometer (Cary 50, Varian®, Milan, Italy) operating in the range of 400–750 nm. The UV-Vis measurements were conducted every 10 min.

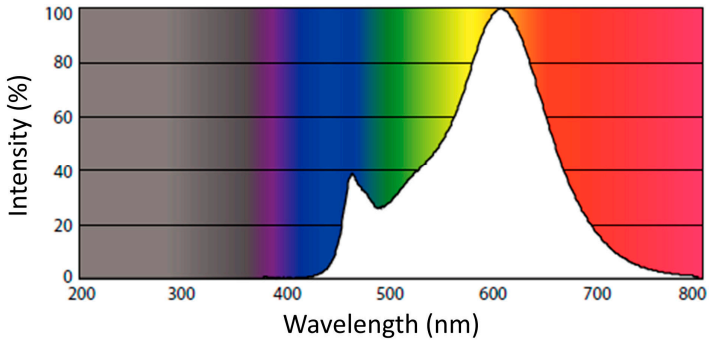

Figure 1. Emission spectrum of the light source provided by the manufacturer.

The efficiency of the dye degradation by the synthesized Ag NPs was calculated as (Equation (2)):

$$\eta(\%) = (1 - C/C_0)100, \quad (2)$$

where η is the degradation efficiency, C_0 is the initial BBR dye concentration, and C is the final concentration of the dye at the end of the degradation period.

According to the literature [20], the data obtained were interpreted through the pseudo-first-order reaction model according to the Equation (3):

$$\frac{dC}{dt} = -k_{app}C, \quad (3)$$

which, once solved, provides the following time evolution law for the dye concentration:

$$C = C_0 \exp(-k_{app}t) \quad (4)$$

where $t(min)$ is the time and $k_{app}(min^{-1})$ is the apparent first-order rate constant. It should be noted that such a model encompasses the effects of both adsorption and photocatalysis in the same constant k_{app}. Equation (4) was used to fit the experimental data by tuning the value of k_{app} using the software OriginPro 2021© 9.8.

3. Results and Discussion

3.1. Characterization

The XRD analysis has proven to be an effective method for revealing the crystal structure of Ag NPs to determine their atomic arrangement, providing valuable insights into their physical and chemical properties (Figure 2A). The XRD spectrum of Ag NPs BC revealed the presence of mainly AgCl (COD 9011666 and COD 9011673) and Ag (COD 1100136) phases with organic capping agents at 2theta = 20°. A similar pattern was reported before [21] using sodium alginate. After calcination, only the Ag (COD 1509146) phase was identified in Ag NPs AC. Specifically, the X-ray diffraction (XRD) patterns of Ag-npBC and Ag-npAC exhibited the presence of peaks at 2θ = 38.2°, 44.4°, 64.6°, 77.5°, and 81.6°, which correspond to the (111), (200), (220), (311), and (222) planes of the Ag phase, respectively. The phase is correctly identified as face-centered cubic Ag, with calculated lattice parameters of 4.075 Å for Ag-npBC and 4.070 Å for Ag-npAC, which are close to the reference values (COD records).

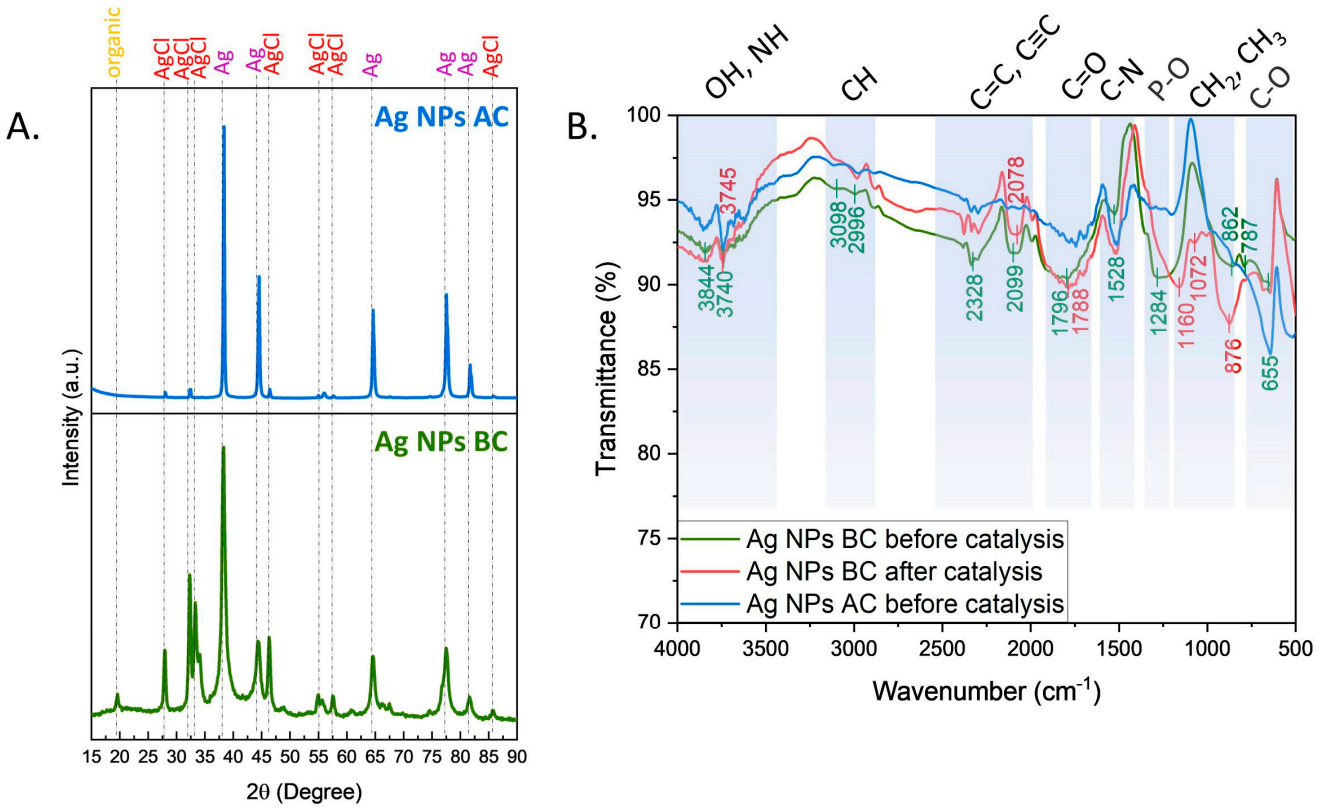

Figure 2. Crystallographic and spectroscopic analyses (**A**) XRD, (**B**) FTIR, BC—before calcination, and AC—after calcination.

The crystallite size of the Ag nanoparticles before (BC) and after calcination (AC) was estimated through the application of Scherrer's formula applied only to the most intense and best-defined peaks (Table S1 and Table S2), resulting in an approximate value of 11.79 nm and 24.60 nm for Ag-NpBC and Ag-NpAC, respectively.

The Williamson and Hall (W&H) method was employed to discern the influence of size and strain on the broadening of the XRD signals. From the W&H plot, it was found that the strain is about 0.093% in the samples after calcination, which is lower than the 0.18% obtained for the samples before calcination, because of the lattice rearrangement and recrystallisation induced by the heat treatment. Correspondingly, the calcination treatment, and the related reduction in microstrain, causes an increase in the crystallite size up to 35.8 nm for Ag-npAC. This value is greater than that predicted by Scherrer's method (24.6 nm), which ignores lattice distortions and is typically better suited to highly isotropic systems with zero strain.

The synthesis mechanism of Ag NPs was studied previously and revealed the involvement of methylamine, diethanolamine, and ethanamine as reducing and stabilizing agents [11]. The phase transition and increase in the crystalline size signify the important role of metabolites in stabilizing the structure. Both the AgCl and Ag phases in Ag NPs have been reported as a result of intracellular synthesis using *Dunaliella salina* and *Scenedesmus* sp. [22,23]. In the current study, the metabolites from the cell were successfully released during extract preparation and the synthesis occurred extracellularly, which decreased the time needed to obtain the product. The organic coating on the surface of the Ag NPs was further examined by FTIR analysis.

The FTIR technique showed an abundance of functional groups on the surface of the Ag NPs such as OH, NH, C=C, C≡C, C=O, C-N, P-O, CH_2, CH_3, and C-O, originating from the *S. pluvialis* extract used for the synthesis [11,24]. The spectra of the Ag NPs BC before and after catalysis display the difference in intensity, mainly in the wavenumber areas attributed to the C=C, C≡C and CH_2, CH_3 groups, which confirms their involvement in

the photocatalytic generation of radicals. The Ag NPs AC exhibit a higher transmittance intensity compared with the Ag NPs BC, which proves partial removal of the organic content due to the calcination. The microalgae extract used in the synthesis contains various organic compounds, such as proteins, polysaccharides, and phenolic compounds. The organic molecules play a dual role: they act as reducing agents, facilitating the reduction of metal ions to form nanoparticles, and as stabilizing agents, capping the nanoparticle surfaces to prevent agglomeration. The organic groups from the extract, such as hydroxyl, carboxyl, and amine groups, remain attached to the surface of the nanoparticles, contributing to their stability and influencing their surface properties during catalytic processes.

The morphological properties of the obtained Ag NPs were studied using SEM and EDX analyses (Figure 3). The obtained Ag NPs BC are spherical or quasi-spherical in shape with silver, chlorine, oxygen, carbon, phosphorus, and sulfur in their structure with homogeneous distributions. The Ag NPs AC are more agglomerated or coalescent while maintaining the tendency toward a spherical or quasi-spherical shape. In the elemental analysis of Ag NPs AC, only silver, oxygen, carbon, and phosphorous were detected with homogenous distributions. Due to calcination, the organic content was partially removed, which decreased the Ag NPs' stability and caused the agglomeration of the material. During calcination, particles gain enough thermal energy to overcome surface energy barriers, which can lead to particle migration and fusion. As the temperature increases, the nanoparticles tend to reduce their surface area to minimize the overall energy of the system. The reduction often causes individual particles to merge or cluster together, forming larger aggregates [25]. Additionally, surface diffusion or sintering processes can occur during calcination, where atoms or ions move across particle surfaces, leading to the coalescence of neighboring particles.

The TEM analysis of the Ag NPs BC reveals a population of well-dispersed particles with predominantly spherical or quasi-spherical shapes. The low degree of agglomeration can be attributed to the organic compounds in the microalgae extract, which serve as natural capping agents. The organic molecules, likely proteins, polysaccharides, and phenolic compounds, form a protective layer around the nanoparticles, visible as a thin halo in the TEM images. The observed capping effect stabilizes the nanoparticles by preventing particle–particle interactions and inhibiting coalescence, leading to a well-dispersed system. Following calcination, a marked change in the morphology and size distribution of the Ag NPs AC is observed in the TEM images. The calcination process removes the organic capping layer, as evidenced by the absence of the protective halo previously seen around the nanoparticles. Without the stabilizing effect of the organic matrix, the nanoparticles become more prone to coalescence and aggregation, forming larger clusters. Although the individual nanoparticles generally retain their spherical or quasi-spherical shapes, the increased particle–particle interactions due to agglomeration are visible. The thermal-induced growth and agglomeration are consistent with the enhanced crystallinity observed in the XRD results post-calcination.

The thermal behavior of the obtained products was examined by the TGA technique (Figure 4A–C). The Ag NPs BC showed three stages of mass loss at the ranges 25–250 °C, 250–550 °C, and 550–1000 °C. The first decrease with a 7.5% weight loss and DTG peak at 182 °C can be attributed to the loss of physically adsorbed water molecules or decomposition of temperature-sensitive organic compounds [26]. The removal of organic compounds progressed in the next stage, with a 4.9% weight loss and DTG peak at 380 °C when the phenolic compounds decomposed on the surface [27]. Then, the weight decreased by 5.7% with the DTG peak close to 1000 °C, signifying the decomposition of higher-molecular-weight compounds or molecular oxygen removal [11,26]. The final weight of the Ag NPs BC was recorded at around 80%. In addition, the DTA analysis provided information about the exothermic nature of the organic content decomposition, with various peaks at 25–600 °C signifying the abundance of compounds on the surface of the Ag NPs BC. The endothermic peak at 960 °C is attributed to the melting point of silver present in the structure [28].

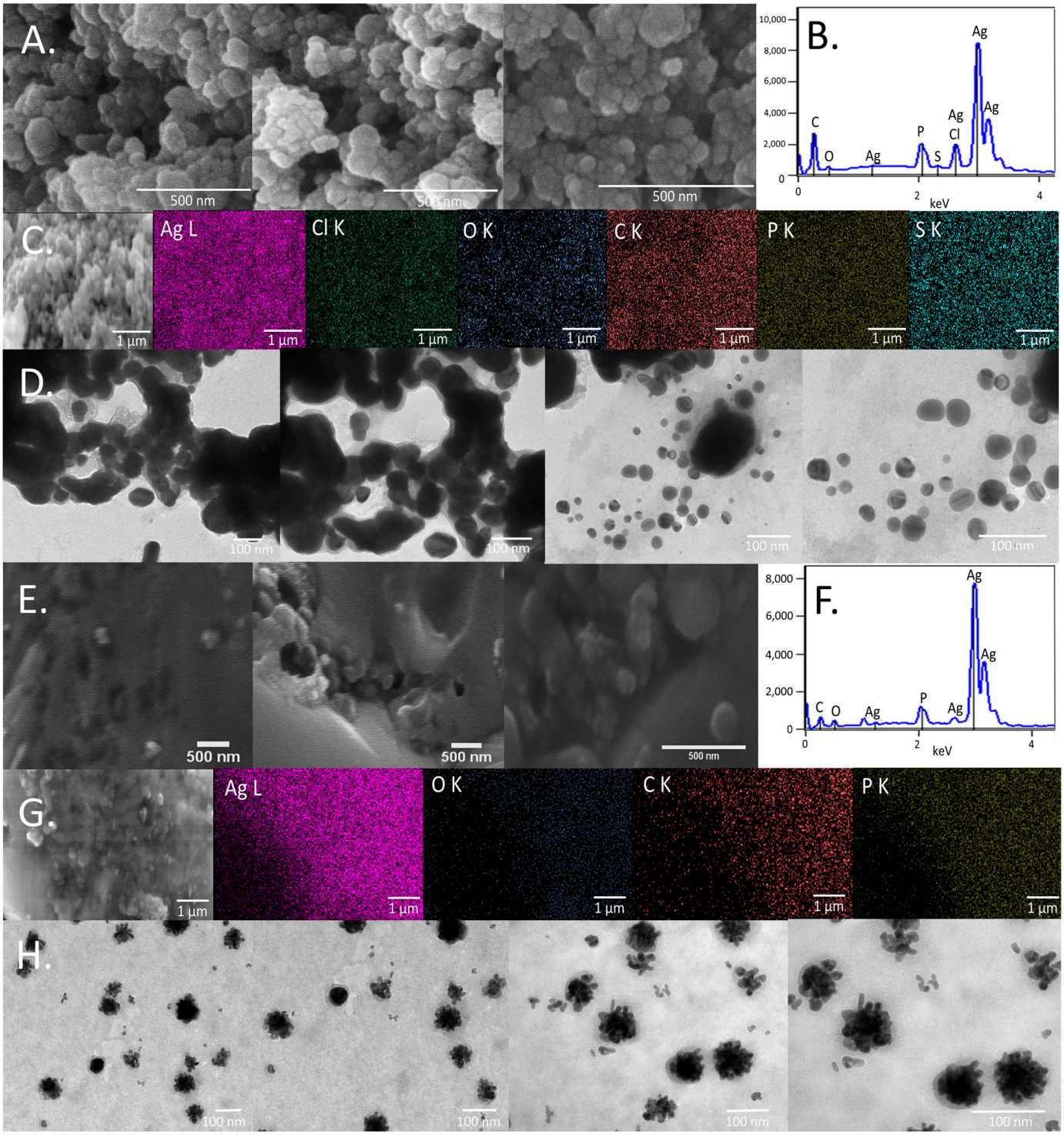

Figure 3. Microscopy analysis: (**A**) SEM of Ag NPs BC, (**B**) EDX spectrum of Ag NPs BC, (**C**) EDX mappings of Ag NPs BC, (**D**) TEM of Ag NPs BC, (**E**) SEM of Ag NPs AC, (**F**) EDX spectrum of Ag NPs AC, (**G**) EDX mappings of Ag NPs AC, and (**H**) TEM of Ag NPs AC.

The thermal properties of the Ag NPs AC were also assessed. The slight weight loss of 0.5% with the DTG peak at 135 °C can be related to the water loss or oxidation of the remaining organic content. The most significant weight loss of 4.5% with a DTG peak at around 1000 °C is similar to the Ag NPs BC. The weight at the end of the measurement was recorded at around 95%. The DTA analysis revealed a low-intensity exothermic peak at around 45 °C and an endothermic peak at 960 °C, which represents the melting point of

silver. The TGA analysis confirmed the difference in the amount of organic content in Ag NPs BC and Ag NPs AC. Moreover, the metabolites showed different thermal behaviors manifesting in the presence of many peaks, especially in the DTA analysis, which proves the abundance of molecules as observed in the FTIR analysis.

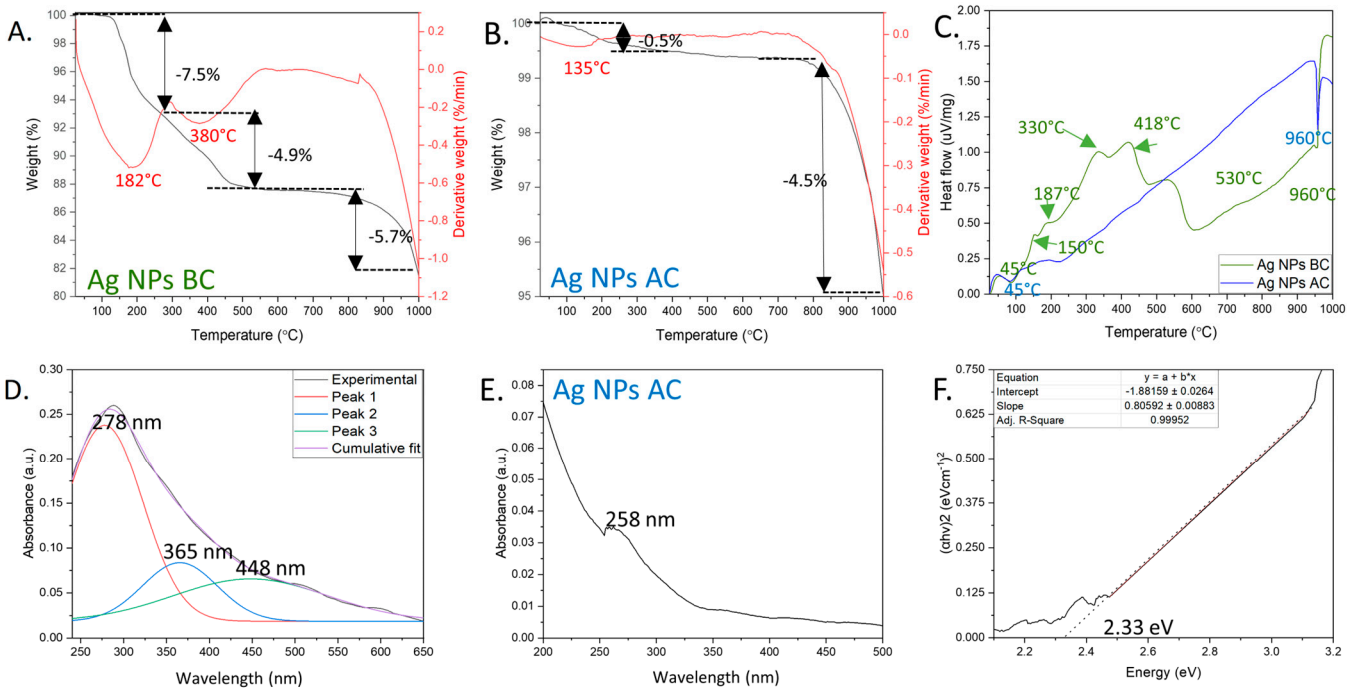

Figure 4. Thermal and optical properties of Ag NPs: (**A**) TG and DTG of Ag NPs BC, (**B**) TG and DTG of Ag NPs AC, (**C**) DTA of Ag NPs BC and Ag NPs AC, (**D**) UV-Vis spectrum of Ag NPs BC, (**E**) UV-Vis spectrum of Ag NPs AC, and (**F**) Tauc plot of Ag NPs BC.

The optical properties of Ag NPs BC and Ag NPs AC were analyzed using UV-Vis spectroscopy (Figure 4D,E). Plasmonic nanoparticles such as Ag NPs can exhibit surface plasmon resonance when electrons in the conductive band excited at a specific wavelength undergo collective oscillation. The effect enables strong light scattering and absorption, which are important for the photocatalytic activity. The Ag NPs BC displayed a broad absorption band, which, after deconvolution, can be divided into three separate peaks. The peaks at 278 nm and 365 nm can be attributed to the organic molecules present on the surface. In the literature, the metabolites present in the extract were previously detected in a similar range [29]. Moreover, the peak at 448 nm can be assigned to the characteristic Ag NP surface plasmon resonance typically found in the 400–500 nm range [30]. The results show the potential of Ag NPs BC to be photoactivated in the visible light spectrum.

The obtained Ag NPs AC displayed one peak at 258 nm, which might be a result of structural defects and a change in the electronic state due to the calcination procedure [31]. A similar behavior has been reported before as a result of electronic transition to metallic Ag [31], which is correlated with the XRD findings. Consequently, the calcination procedure might have impaired the photocatalytic activity of Ag NPs AC.

The optical properties were also characterized by the calculation of the bandgap energy. The parameter is defined as an energy difference between the highest occupied energy state in the valence band and the lowest unoccupied energy state in the conduction band. A low bandgap value facilitates the ability of the material to absorb light, generate electron–hole pairs, and initiate photocatalytic reactions. Based on the UV-Vis absorption, the bandgap energy for Ag NPs BC was calculated at 2.33 eV (Figure 4F). The typical bandgap energy for Ag NPs depends on their size, shape, and surrounding environment but generally ranges from 2.0 to 3.5 eV [32,33]. The confinement of electrons in Ag NPs, especially at the nanoscale, leads to quantum effects, resulting in a measurable bandgap that influences

their optical and electronic properties. The tunable bandgap allows Ag NPs to absorb and respond to visible and ultraviolet light, making them useful in photocatalysis, while bandgap energies around 2.2–2.5 eV are particularly relevant for visible light activation. A similar bandgap value has been reported for Ag NPs synthesized using *Hagenia abyssinica (Brace) JF. Gmel*. plant extract [34].

3.2. Photocatalytic Activity

The linear correlation between BBR dye absorbance and concentration is shown in Figure S1. The BBR dye degradation activity of Ag NPs BC was first analyzed in dark conditions (Figures 5 and S2).

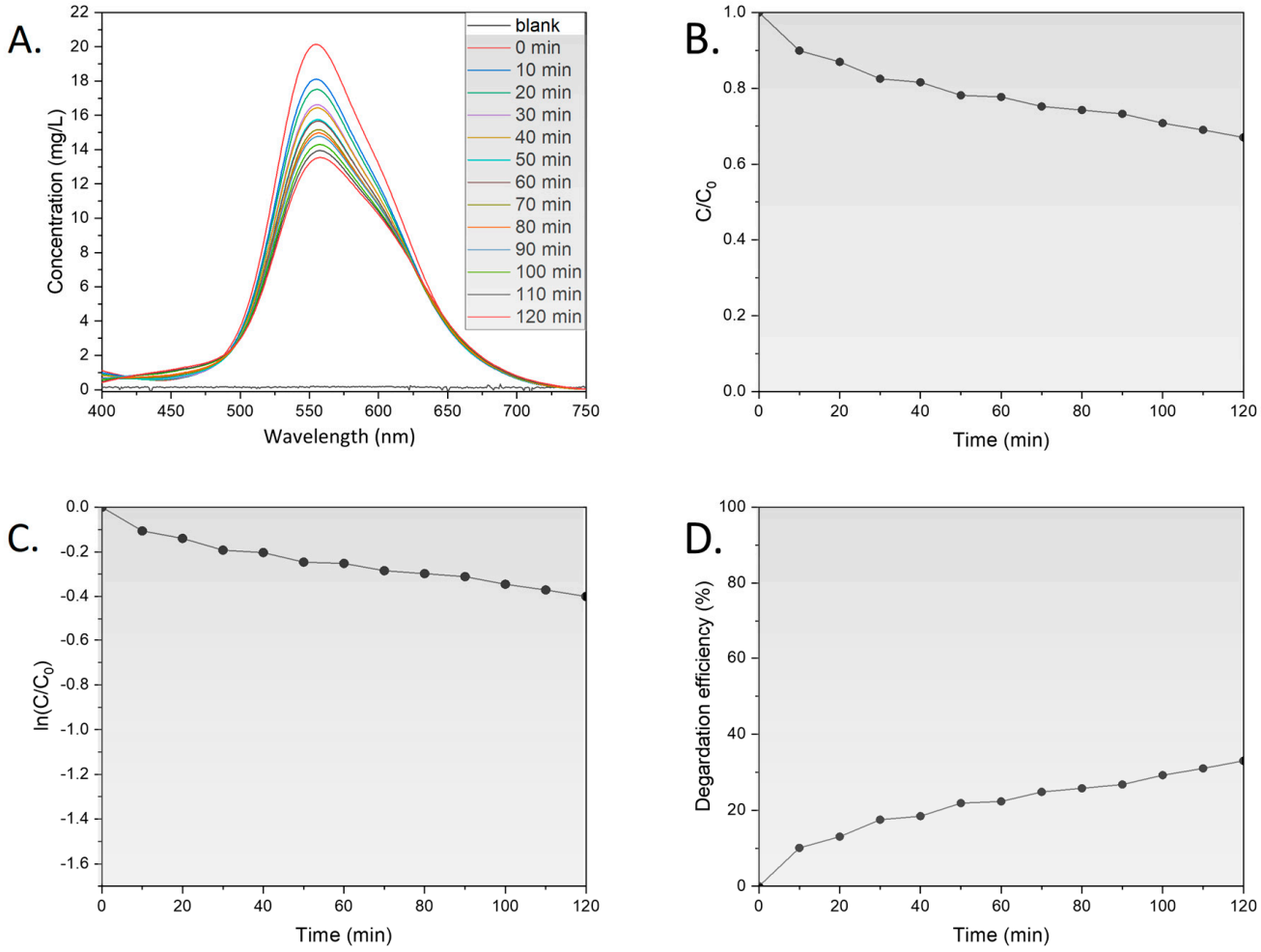

Figure 5. Degradation of BBR dye in the dark: (**A**) UV-Vis spectral changes for the degradation of dye, (**B**) changes in dye concentration, (**C**) pseudo-first-order kinetic plot, and (**D**) percentage degradation efficiency. Reaction conditions: dye concentration: 21 mg/L, Ag NPs BC concentration: 1000 mg/L, and pH: 7.

The highest decrease in dye concentration was recorded at around 30 min, followed by a further slight concentration reduction. The interplay between the dye and Ag NPs BC can be described as physisorption, which is mainly connected with weak van der Waals forces [35]. At the end of the measurement, around 33% of the dye molecules were degraded and the k_{app} value was recorded as 0.00380 min^{-1}. In the subsequent experiments, the reaction was subjected to 30 min in the dark at the beginning to allow for a more precise evaluation of the tested factors on the photocatalytic activity of the Ag NPs BC.

3.2.1. Influence of Light

The initial evaluation of the photocatalytic activity of the Ag NPs BC involved the assessment of various levels of light intensities of 75, 150, and 300 µmol/m^2/s (Figures 6A, S3 and S4). In photocatalysis, electron–hole pair production relies on light exposure intensity and is a crucial step for creating active radicals to degrade pollutants [36]. As light intensity increases, more electrons transition from valence to conduction bands, resulting in the generation of hydroxyl or oxygen radicals [37]. In this series of experiments, the concentration of the BBR dye was measured with time to evaluate the performance of the Ag NPs BC.

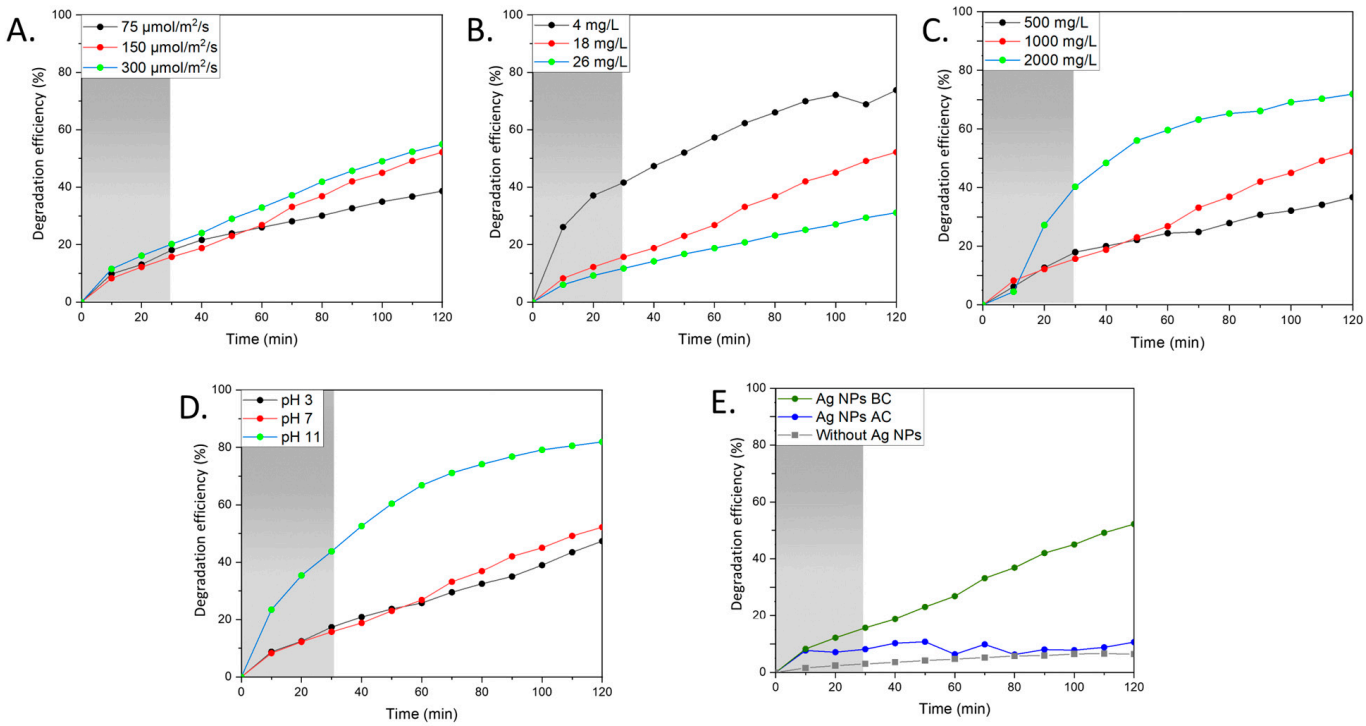

Figure 6. Percentage degradation efficiencies at different operating conditions: (**A**) light intensities, (**B**) dye concentration, (**C**) catalyst concentration, (**D**) pH, and (**E**) calcination.

The lowest tested light intensity resulted in the lowest decrease in the BBR dye concentration with a degradation efficiency of around 39% and k_{app} value of 0.00326 min^{-1}. The increase in light intensity to 150 µmol/m^2/s revealed a significant increase in degradation efficiency to around 52.2% and a k_{app} value of 0.00595 min^{-1}. A further increase in light intensity to 300 µmol/m^2/s showed only a slight increase in degradation efficiency to around 55% with a k_{app} value of 0.00632 min^{-1}. The results can be explained in the context of the quantum yield of photodegradation, which is described as the ratio of absorbed photons that result in a molecular reaction to the total number of absorbed photons [37]. A high quantum yield increases the likelihood of a molecular reaction, while the energy in a low quantum yield can be converted to heat or fluorescence [37]. Overall, the results show the important role of light intensity for the photocatalytic activity of Ag NPs BC.

3.2.2. Influence of Dye Concentration

The light intensity can also be influenced by the concentration of the BBR dye in the solution. The light illuminating the system can also be absorbed by the BBR dye molecules, which decreases the number of photons reaching the catalyst surface and leading to the generation of fewer radicals. The effect of various BBR dye concentrations in the range 4–26 mg/L on the photocatalytic activity of Ag NPs BC is presented in Figures 6B, S5 and S6. As expected, the lowest concentration of the BBR dye re-

sulted in the highest decrease in the concentration with time, with a degradation efficiency around 73.8% and k value of 0.00986 min^{-1}. The increase in the concentration to 16 mg/L showed a decrease in the degradation efficiency at around 52.2% with a k_{app} value of 0.00632 min^{-1}. The highest tested BBR dye concentration revealed the degradation efficiency around 31% with a k_{app} value of 0.00276 min^{-1}. The high concentration of the BBR dye in the solution might not only impart light scattering but also result in the competing action of the molecules for access to the active sites on the catalyst surface, resulting in agglomeration [38]. However, usually the BBR dye concentration in the wastewater is low due to the multiple washings [39], which shows the potential of Ag NPs BC for the removal of BBR dye.

3.2.3. Influence of Catalyst Dosage

The access to the active sites on the surface of Ag NPs BC was tested by measuring the BBR dye concentration in the presence of various catalyst concentrations in the range 500–2000 mg/L (Figures 6C, S7 and S8). As expected, the tested lowest catalyst dosage of 500 mg/L resulted in the lowest decrease in the BBR dye concentration with a degradation efficiency of 36.7% and k_{app} value of 0.00272 min^{-1}. A further increase in the catalyst dosage raised the degradation efficiency to around 52.2% and 71.9% with k_{app} values of 0.00595 min^{-1} and 0.00933 min^{-1} for 1000 mg/L and 2000 mg/L, respectively. The results show the important role of active sites on the Ag NPs' BC surface to improve the photocatalytic degradation of BBR dye [38]. However, it has been reported that the trend only holds up to certain limits as the excess amount of added catalyst might increase turbidity, which affects the light scattering [40].

3.2.4. Influence of pH

The next tested factor for the photocatalytic activity of Ag NPs BC was the pH of the solution in the range 3–11 (Figures 6D, S9 and S10). In acidic conditions, the decrease in the BBR dye was the least prominent and the degradation efficiency was recorded at around 47.3% with a k_{app} value of 0.00443 min^{-1}. The neutral pH showed a degradation efficiency of around 52.2% with a k_{app} value of 0.00595 min^{-1}. The alkaline conditions resulted in the degradation efficiency of 81.9% and k_{app} constant of 0.01496 min^{-1}. Describing the role of pH can be challenging, primarily due to the pH dependence of many processes such as the electrostatic interactions of the catalyst surface with other molecules, such as the solvent, substrate, and generated charged radicals [41]. In alkaline conditions, the surface charge of Ag NPs BC often becomes more negative, which increases the electrostatic attraction between the nanoparticles and the positively charged dye molecules, leading to more efficient adsorption. Additionally, a higher pH can promote the formation of hydroxyl ions (OH^-), which are key precursors for generating highly reactive hydroxyl radicals (•OH) during the photocatalytic process. At an elevated pH, the conduction band electrons of Ag NPs BC may become more reactive due to the increased availability of OH^-, leading to more efficient reduction reactions. Furthermore, in alkaline conditions, the generation of superoxide radicals ($O_2{}^-$•) from dissolved oxygen is favored, which can also contribute to dye degradation. The stability of nanoparticles may improve in basic environments, reducing the likelihood of nanoparticle aggregation and thereby maintaining a higher surface area for catalysis. In the present study, increased BBR removal with increasing pH could relate to the higher accessibility of hydroxyl anions, which, after interactions with positive holes on the catalyst, can result in the elevated concentration of hydroxyl radicals [42]. The effect might persist until a certain pH, when the radical rate formation is decreased due to the Coulomb repulsion between the negatively charged surface of the catalyst and hydroxyl anions [43].

3.2.5. Influence of Calcination

In the final set of experiments, the influence of calcination and the resulting removal of organic content was tested for photocatalytic activity (Figures 6E, S11 and S12). The

Ag NPs AC showed a minimal decrease in BBR dye concentration with a degradation efficiency around 10.7% and k_{app} value of 0.00009 min^{-1}. Moreover, before the treatment, the degradation efficiency was recorded around 52.2% with a k_{app} value of 0.00595 min^{-1}. The BBR dye without any catalyst was degraded by around 6.5% with a k_{app} value of 0.00049 min^{-1}. In the previous study, the calcination at 150 °C managed to reduce the antifungal activity of Ag NPs synthesized using *S. platensis* extract [11]. The increased calcination temperature might cause more structural defects, which can result in different properties of the material as shown in the UV-Vis findings. In addition, Ag/Ag_2O calcined at 600 °C exhibited photocatalytic activity in the UVA spectrum, which might increase the cost of the photocatalytic removal [44].

3.2.6. Mechanism of Dye Degradation

It is widely acknowledged that photocatalysis entails a sequence of reactions between the catalyst and pollutant [37,42,45]. The scheme of the BBR dye degradation process is shown in Figure 7. First, the electrons from the valence band are excited into the conduction band upon light irradiation (Equation (5)), which generates positively charged holes (h^+). Then, the holes react with water molecules, producing H^+ and •OH radicals (6). The electrons after excitation convert the molecular oxygen in the solution into $\bullet O_2^-$ (7), reacting with water molecules to produce •OOH (8). After rearranging to H_2O_2 (9), it reacts with $\bullet O_2^-$ to produce •OH (10), which can also be generated after the reaction of hydroxyl ions with holes (11). The above reactions are described below (Equations (5)–(11)).

$$\text{Photocatalyst surface} + hv \rightarrow \text{electron } (e^-) + \text{hole } (h^+) \quad (5)$$

$$h^+ + H_2O \rightarrow H^+ + \bullet OH \quad (6)$$

$$e^- + O_2 \rightarrow \bullet O_2^- \quad (7)$$

$$\bullet O_2^- + H_2O \rightarrow \bullet OOH + OH^- \quad (8)$$

$$2\bullet OOH \rightarrow H_2O_2 + O_2 \quad (9)$$

$$H_2O_2 + \bullet O_2^- \rightarrow \bullet OH + O_2 + OH^- \quad (10)$$

$$OH^- + h+ \rightarrow \bullet OH \quad (11)$$

BBR is a synthetic dye designed for its color stability and longevity, which poses a challenge for degradation. It belongs to the class of triphenylmethane dyes, containing three phenyl rings linked to a central carbon atom [46]. The presence of conjugated double bonds in the aromatic rings leads to electron delocalization with resonance stabilization, which allows for electronic charge distribution and prevents the formation of reactive sites [47,48]. Moreover, BBR dye does not contain highly labile functional groups that could be easily cleaved, which reduces its susceptibility to chemical breakdown [49]. Thus, this AOP is considered a promising method to degrade BBR dye.

The BBR degradation pathway was studied based on the ultrasound treatment, which also includes the generation of hydroxyl radicals [50]. Based on the LC-Q-TOF-MS analysis, two degradation pathways were proposed. One involves OH addition and the other involves hydrogen abstraction followed by a disproportionation/hydroxylation reaction [50]. Then, the molecules undergo a series of reactions, such as bond breakage, oxidative cleavage, or demethylation. In total, 13 transformed products were identified; however, the molecules could be further transformed by ring opening and other oxidative cleavages, resulting in the formation of inorganic ions, carbon dioxide, and water as part of the mineralization process [50]. The degradation pathway was also studied in river water, revealing its independence from the presence of inorganic ions [51].

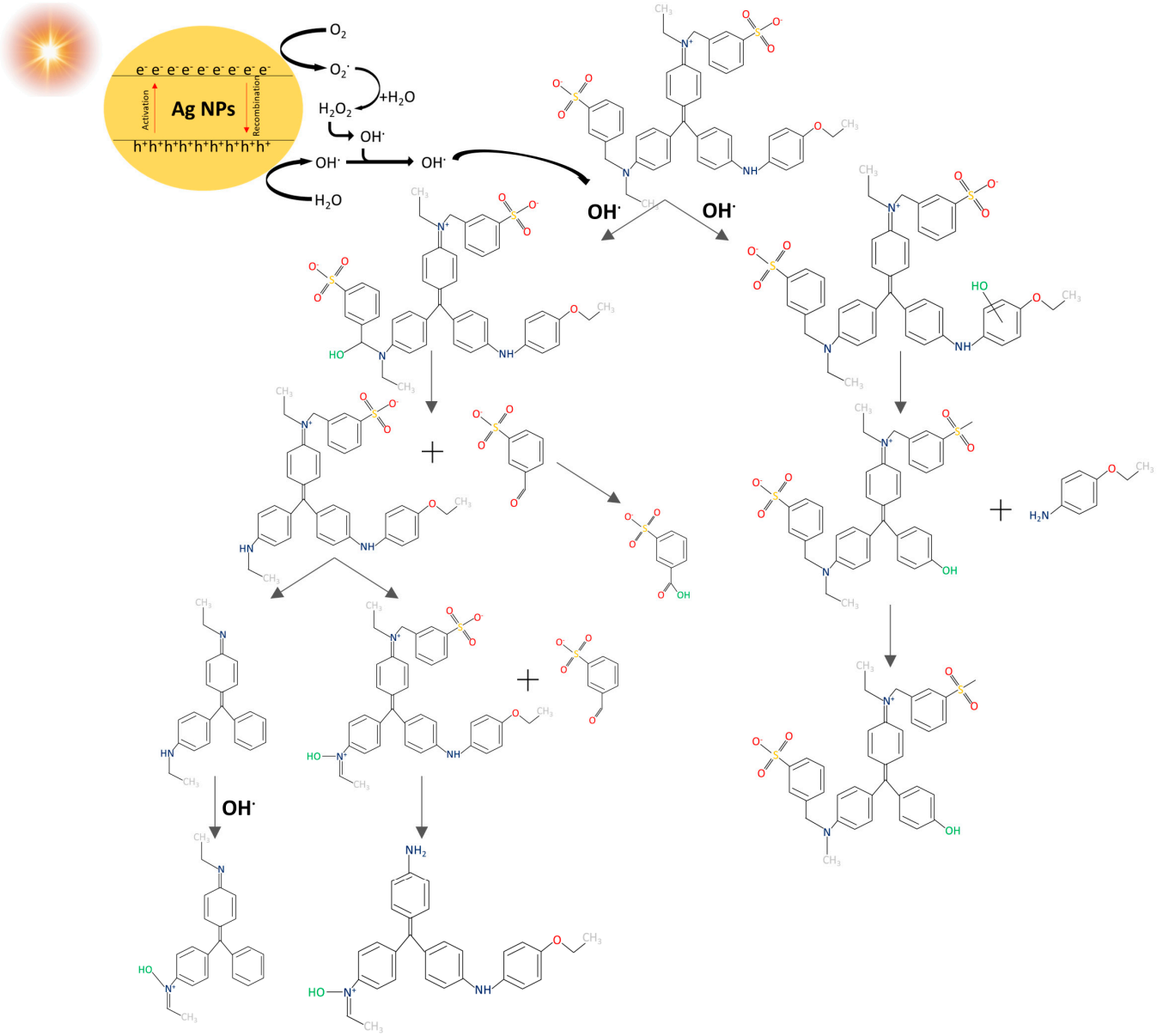

Figure 7. Mechanism of BBR dye degradation, adapted from [50].

Finally, while the results so far discussed confirm the potentialities of the investigated green technique for the synthesis of Ag NPs capable to effectively degrade BBR, further analyses should be performed to gain insight into specific aspects, such as the photocurrent curve [52] and the long-term stability of the obtained photocatalyst as reported in [53,54]. Work is underway along these lines.

4. Conclusions

The production of efficient and stable photocatalysts is of utmost importance for the successful remediation of water pollution. Achieving this goal requires a comprehensive understanding of the underlying chemical processes, as well as an analysis of the various factors that can influence the performance of photocatalytic systems. In this study, the methanolic extract of *S. platensis* was used to synthesize Ag NPs BC and Ag NPs AC. An XRD analysis showed AgCl and Ag phases in Ag NPs BC with a crystalline size of 11.79 nm, while only the Ag phase was present in Ag NPs AC with a size of 24.60 nm. FTIR confirmed functional groups from the extract on the surface of Ag NPs BC. SEM showed spherical or quasi-spherical morphologies, and EDX supported the FTIR results. A TGA

revealed differing thermal stability between the nanoparticles, and UV-Vis indicated visible light activation of Ag NPs BC with a bandgap of 2.33 eV. Photocatalytic tests against BBR dye under visible light showed 81.9% degradation efficiency in alkaline conditions, with a proposed mechanism involving hydroxyl radicals. This study highlights *S. platensis* as a source for synthesizing photocatalytically active products.

Supplementary Materials: The following supporting information can be downloaded at: https://www.mdpi.com/article/10.3390/su16208758/s1, Table S1: XRD values and crystalline size of the detected phases in Ag NPs BC; Table S2: XRD values and crystalline size of the detected phases in Ag NPs AC; Figure S1: Calibration line: (A) absorbance profile of BBR dye at different concentrations, and (B) plot of concentration at the maximum absorbance peak at 555 nm; Figure S2: Rate constant in the dark conditions. Fitted parameters were calculated based on the dotted red plot; Figure S3: Rate constant at different light intensities: (A) dark, (B) 75 µmol/m^2/s, (C) dark, (D) 150 µmol/m^2/2, (E) dark, and (F) 300 µmol/m^2/s. Fitted parameters were calculated based on the dotted red plot; Figure S4: Rate constant at different dye concentrations: (A) 4 mg/L in the dark, (B) 4 mg/L in the light, (C) 18 mg/L in the dark, (D) 18 mg/L in the light, (E) 26 mg/L in the dark, and (F) 26 mg/L in the light. Fitted parameters were calculated based on the dotted red plot; Figure S5: Rate constant in different catalyst loadings: (A) 500 mg/L in the dark, (B) 500 mg/L in the light, (C) 1000 mg/L in the dark, (D) 1000 mg/L in the light, (E) 2000 mg/L in the dark, and (F) 2000 mg/L in the light. Fitted parameters were calculated based on the dotted red plot; Figure S6: Rate constant at different pH: (A) pH 3 in the dark, (B) pH 3 in the light, (C) pH 7 in the dark, (D), pH 7 in the light, (E) pH 11 in the dark, and (F) pH 11 in the light. Fitted parameters were calculated based on the dotted red plot; Figure S7: Rate constant: (A) Ag NPs BC in the dark, (B) Ag NPs BC in the light, (C) Ag NPs AC in the dark, (D) Ag NPs AC in the light, (E) without Ag NPs in the dark, and (F) without Ag NPs in the light. Fitted parameters were calculated based on the dotted red plot; Figure S8. Rate constant in different catalyst loadings, (A) 500 mg/L in the dark, (B) 500 mg/L in the light, (C) 1000 mg/L in the dark, (D) 1000 mg/L in the light, (E) 2000 mg/L in the dark, (F) 2000 mg/L in the light. Fitted parameters were calculated based on the dotted red plot; Figure S9 Influence of pH on the photocatalytic activity (A-C) UV–Vis spectral changes in the varying pH, (D) changes in dye concentration. Reaction conditions: dye concentration: 18–19 mg/L, Ag NPs BC concentration: 1000 mg/L, light intensity: 150 µmol/m2/s; Figure S10. Rate constant in the different pH, (A) pH 3 in the dark, (B) pH 3 in the light, (C) pH 7 in the dark, (D), pH 7 in the light, (E) pH 11 in the dark, (F) pH 11 in the light. Fitted parameters were calculated based on the dotted red plot; Figure S11 Influence of calcination on the photocatalytic activity (A) UV–Vis spectral changes before calcination, (B) UV–Vis spectral changes after calcination, (C) UV–Vis spectral changes without catalyst, (D) changes in dye concentration. Reaction conditions: dye concentration: 17–22 mg/L, Ag NPs BC concentration: 1000 mg/L, light intensity: 150 µmol/m2/s, pH: 7; Figure S12. Rate constant (A) Ag NPs BC in the dark, (B) Ag NPs BC in the light, (C) Ag NPs AC in the dark, (D) Ag NPs AC in the light, (E) without Ag NPs in the dark, (F) without Ag NPs in the light. Fitted parameters were calculated based on the dotted red plot.

Author Contributions: Conceptualization, A.S., G.F. and A.C.; methodology, A.S., G.F., F.D., R.L. and A.C.; software, A.S.; validation, A.S. and A.C.; formal analysis, A.S.; investigation, A.S., G.F., F.L. and R.L.; resources, F.D., F.L., N.L., G.C., R.L. and A.C.; data curation, A.S.; writing—original draft preparation, A.S.; writing—review and editing, A.S., G.F., F.D., R.L., N.L., G.C. and A.C.; visualization, A.S.; supervision, A.C.; project administration, G.C. and A.C.; funding acquisition, G.C. All authors have read and agreed to the published version of the manuscript.

Funding: This research received no external funding.

Institutional Review Board Statement: Not applicable.

Informed Consent Statement: Not applicable.

Data Availability Statement: The original contributions presented in the study are included in the article and in the Supplementary Material; further inquiries can be directed to the corresponding authors.

Acknowledgments: A.S. performed her activity in the framework of the International PhD in Innovation Sciences and Technologies at the University of Cagliari, Italy. The precious help of Dominika

Moravcova during the experimental activity is also gratefully acknowledged. We acknowledge the CeSAR (Centro Servizi d'Ateneo per la Ricerca) of the University of Cagliari, Italy, and Andrea Ardu for assistance with the Transmission Electron Microscopy TEM Jeol JEM 1400 Plus.

Conflicts of Interest: The authors declare no conflicts of interest.

References

1. Islam, T.; Repon, M.R.; Islam, T.; Sarwar, Z.; Rahman, M.M. Impact of Textile Dyes on Health and Ecosystem: A Review of Structure, Causes, and Potential Solutions. *Environ. Sci. Pollut. Res.* **2022**, *30*, 9207–9242. [CrossRef] [PubMed]
2. Tomar, T.; Kahandawala, N.; Kaur, J.; Thounaojam, L.; Choudhary, I.; Bera, S. Bioremediation of Synthetic Dyes from Wastewater by Using Microbial Nanocomposites: An Emerging Field for Water Pollution Management. *Biocatal. Agric. Biotechnol.* **2023**, *51*, 102767. [CrossRef]
3. Ahmadian, M.; Jaymand, M. Interpenetrating Polymer Network Hydrogels for Removal of Synthetic Dyes: A Comprehensive Review. *Coord. Chem. Rev.* **2023**, *486*, 215152. [CrossRef]
4. Iqbal, A.; Yusaf, A.; Usman, M.; Hussain Bokhari, T.; Mansha, A. Insight into the Degradation of Different Classes of Dyes by Advanced Oxidation Processes; a Detailed Review. *Int. J. Environ. Anal. Chem.* **2023**, 1–35. [CrossRef]
5. Mohod, A.V.; Momotko, M.; Shah, N.S.; Marchel, M.; Imran, M.; Kong, L.; Boczkaj, G. Degradation of Rhodamine Dyes by Advanced Oxidation Processes (AOPs)—Focus on Cavitation and Photocatalysis—A Critical Review. *Water Resour. Ind.* **2023**, *30*, 100220. [CrossRef]
6. Park, S.; Keum, Y.; Park, J. Ti-Based Porous Materials for Reactive Oxygen Species-Mediated Photocatalytic Reactions. *Chem. Commun.* **2022**, *58*, 607–618. [CrossRef]
7. Wang, Q.; Zhu, S.; Zhao, S.; Li, C.; Wang, R.; Cao, D.; Liu, G. Construction of Bi-Assisted Modified CdS/TiO_2 Nanotube Arrays with Ternary S-Scheme Heterojunction for Photocatalytic Wastewater Treatment and Hydrogen Production. *Fuel* **2022**, *322*, 124163. [CrossRef]
8. Wang, Q.; Zhao, S.; Zhao, Y.; Deng, Y.; Yang, W.; Ye, Y.; Wang, K. Construction of Z-Scheme Bi_2O_3/CeO_2 Heterojunction for Enhanced Photocatalytic Capacity of TiO_2 NTs. *Spectrochim. Acta-Part A Mol. Biomol. Spectrosc.* **2024**, *304*, 123405. [CrossRef]
9. Vidyasagar, N.; Patel, R.R.; Singh, S.K.; Singh, M. Green Synthesis of Silver Nanoparticles: Methods, Biological Applications, Delivery and Toxicity. *Mater. Adv.* **2023**, *4*, 1831–1849. [CrossRef]
10. Sidorowicz, A.; Fais, G.; Casula, M.; Borselli, M.; Giannaccare, G.; Locci, A.M.; Lai, N.; Orrù, R.; Cao, G.; Concas, A. Nanoparticles from Microalgae and Their Biomedical Applications. *Mar. Drugs* **2023**, *21*, 352. [CrossRef]
11. Sidorowicz, A.; Margarita, V.; Fais, G.; Pantaleo, A.; Manca, A.; Concas, A.; Rappelli, P.; Fiori, P.L.; Cao, G. Characterization of Nanomaterials Synthesized from Spirulina Platensis Extract and Their Potential Antifungal Activity. *PLoS ONE* **2022**, *17*, e0274753. [CrossRef] [PubMed]
12. Concas, A.; Steriti, A.; Pisu, M.; Cao, G. Experimental and Theoretical Investigation of the Effects of Iron on Growth and Lipid Synthesis of Microalgae in View of Their Use to Produce Biofuels. *J. Environ. Chem. Eng.* **2021**, *9*, 105349. [CrossRef]
13. Concas, A.; Lutzu, G.A.; Turgut Dunford, N. Experiments and Modeling of Komvophoron Sp. Growth in Hydraulic Fracturing Wastewater. *Chem. Eng. J.* **2021**, *426*, 131299. [CrossRef]
14. Concas, A.; Pisu, M.; Cao, G. Microalgal Cell Disruption Through Fenton Reaction: Experiments, Modeling and Remarks on Its Effect on the Extracted Lipids Composition. *Chem. Eng. Trans.* **2015**, *43*, 367–372. [CrossRef]
15. Gentscheva, G.; Nikolova, K.; Panayotova, V.; Peycheva, K.; Makedonski, L.; Slavov, P.; Radusheva, P.; Petrova, P.; Yotkovska, I. Application of Arthrospira Platensis for Medicinal Purposes and the Food Industry: A Review of the Literature. *Life* **2023**, *13*, 845. [CrossRef]
16. Ismail, G.A.; Allam, N.G.; El-Gemizy, W.M.; Salem, M.A. The Role of Silver Nanoparticles Biosynthesized by Anabaena Variabilis and Spirulina Platensis Cyanobacteria for Malachite Green Removal from Wastewater. *Environ. Technol.* **2021**, *42*, 4475–4489. [CrossRef]
17. Roja, K.; Mehta, P.; Premalatha, M.; Jeyadheepan, K.; Gopalakrishnan, C.; Meenakshisundaram, N.; Sankaranarayanan, K. Biosynthesized Silver Nanoparticles as Antimicrobial Agents and Photocatalytic Degradation of Methylene Blue. *DDesalination Water Treat.* **2019**, *156*, 292–302. [CrossRef]
18. Gul, A.; Ahmed, D.; Fazil, M.M.; Aslam, T.; Rashid, M.A.; Khan, H.; Ali, A.; Ali, S. Biofabrication of Silver Nanoparticles Using Spirulina Platensis: In Vitro Anti-Coagulant, Thrombolytic and Catalytic Dye Degradation Activity. *Microsc. Res. Tech.* **2023**, *86*, 823–833. [CrossRef]
19. Mohamed, I.M.A.; Dao, V.D.; Barakat, N.A.M.; Yasin, A.S.; Yousef, A.; Choi, H.S. Efficiency Enhancement of Dye-Sensitized Solar Cells by Use of ZrO2-Doped TiO_2 Nanofibers Photoanode. *J. Colloid Interface Sci.* **2016**, *476*, 9–19. [CrossRef]
20. Jiang, Z.; Hu, J.; Zhang, X.; Zhao, Y.; Fan, X.; Zhong, S.; Zhang, H.; Yu, X. A Generalized Predictive Model for TiO_2–Catalyzed Photo-Degradation Rate Constants of Water Contaminants through Artificial Neural Network. *Environ. Res.* **2020**, *187*, 109697. [CrossRef]
21. Nocchetti, M.; Pietrella, D.; Antognelli, C.; Di Michele, A.; Russo, C.; Giulivi, E.; Ambrogi, V. Alginate Microparticles Containing Silver@hydroxyapatite Functionalized Calcium Carbonate Composites. *Int. J. Pharm.* **2024**, *661*, 124393. [CrossRef] [PubMed]

22. Cepoi, L.; Zinicovscaia, I.; Rudi, L.; Chiriac, T.; Turchenko, V. Changes in the Dunaliella Salina Biomass Composition during Silver Nanoparticles Formation. *Nanotechnol. Environ. Eng.* **2022**, *7*, 235–243. [CrossRef]
23. Kashyap, M.; Samadhiya, K.; Ghosh, A.; Anand, V.; Lee, H.; Sawamoto, N.; Ogura, A.; Ohshita, Y.; Shirage, P.M.; Bala, K. Synthesis, Characterization and Application of Intracellular Ag/AgCl Nanohybrids Biosynthesized in Scenedesmus Sp. as Neutral Lipid Inducer and Antibacterial Agent. *Environ. Res.* **2021**, *201*, 111499. [CrossRef] [PubMed]
24. Mecozzi, M.; Pietroletti, M.; Scarpiniti, M.; Acquistucci, R.; Conti, M.E. Monitoring of Marine Mucilage Formation in Italian Seas Investigated by Infrared Spectroscopy and Independent Component Analysis. *Environ. Monit. Assess.* **2012**, *184*, 6025–6036. [CrossRef]
25. Sidorowicz, A.; Yigit, N.; Wicht, T.; Stöger-Pollach, M.; Concas, A.; Orrù, R.; Cao, G.; Rupprechter, G. Microalgae-Derived Co3O4 Nanomaterials for Catalytic CO Oxidation. *RSC Adv.* **2024**, *14*, 4575–4586. [CrossRef]
26. Alzahrani, E.A.; Nabi, A.; Kamli, M.R.; Albukhari, S.M.; Althabaiti, S.A.; Al-Harbi, S.A.; Khan, I.; Malik, M.A. Facile Green Synthesis of ZnO NPs and Plasmonic Ag-Supported ZnO Nanocomposite for Photocatalytic Degradation of Methylene Blue. *Water* **2023**, *15*, 384. [CrossRef]
27. Vera, J.; Herrera, W.; Hermosilla, E.; Díaz, M.; Parada, J.; Seabra, A.B.; Tortella, G.; Pesenti, H.; Ciudad, G.; Rubilar, O. Antioxidant Activity as an Indicator of the Efficiency of Plant Extract-Mediated Synthesis of Zinc Oxide Nanoparticles. *Antioxidants* **2023**, *12*, 784. [CrossRef]
28. Kis, B.; Moacă, E.A.; Tudoran, L.B.; Muntean, D.; Magyari-Pavel, I.Z.; Minda, D.I.; Lombrea, A.; Diaconeasa, Z.; Dehelean, C.A.; Dinu, Ș.; et al. Green Synthesis of Silver Nanoparticles Using Populi Gemmae Extract: Preparation, Physicochemical Characterization, Antimicrobial Potential and In Vitro Antiproliferative Assessment. *Materials* **2022**, *15*, 5006. [CrossRef]
29. Lite, M.C.; Constantinescu, R.R.; Tănăsescu, E.C.; Kuncser, A.; Romaniţan, C.; Lăcătuşu, I.; Badea, N. Design of Green Silver Nanoparticles Based on Primula Officinalis Extract for Textile Preservation. *Materials* **2022**, *15*, 7695. [CrossRef]
30. Ma, Z.; Liu, J.; Liu, Y.; Zheng, X.; Tang, K. Green Synthesis of Silver Nanoparticles Using Soluble Soybean Polysaccharide and Their Application in Antibacterial Coatings. *Int. J. Biol. Macromol.* **2021**, *166*, 567–577. [CrossRef]
31. Baia, L.; Simon, S. UV-VIS and TEM Assessment of Morphological Features of Silver Nanoparticles from Phosphate Glass Matrices. *Mod. Res. Educ. Top. Microsc.* **2007**, *2*, 576–583.
32. Skanda, S.; Bharadwaj, P.S.J.; Datta Darshan, V.M.; Sivaramakrishnan, V.; Vijayakumar, B.S. Proficient Mycogenic Synthesis of Silver Nanoparticles by Soil Derived Fungus Aspergillus Melleus SSS-10 with Cytotoxic and Antibacterial Potency. *J. Microbiol. Methods* **2022**, *199*, 106517. [CrossRef] [PubMed]
33. Joy, J.; Gurumurthy, M.S.; Thomas, R.; Balachandran, M. Biosynthesized AG Nanoparticles: A Promising Pathway for Bandgap Tailoring. *Biointerface Res. Appl. Chem.* **2021**, *11*, 8875–8883. [CrossRef]
34. Ananda Murthy, H.C.; Desalegn Zeleke, T.; Ravikumar, C.R.; Anil Kumar, M.R.; Nagaswarupa, H.P. Electrochemical Properties of Biogenic Silver Nanoparticles Synthesized Using Hagenia Abyssinica (Brace) JF. Gmel. Medicinal Plant Leaf Extract. *Mater. Res. Express* **2020**, *7*, 055016. [CrossRef]
35. Munagapati, V.S.; Wen, H.Y.; Gollakota, A.R.K.; Wen, J.C.; Lin, K.Y.A.; Shu, C.M.; Yarramuthi, V.; Basivi, P.K.; Reddy, G.M.; Zyryanov, G.V. Magnetic Fe_3O_4 Nanoparticles Loaded Guava Leaves Powder Impregnated into Calcium Alginate Hydrogel Beads (Fe3O4-GLP@CAB) for Efficient Removal of Methylene Blue Dye from Aqueous Environment: Synthesis, Characterization, and Its Adsorption Performance. *Int. J. Biol. Macromol.* **2023**, *246*, 125675. [CrossRef] [PubMed]
36. Heredia Deba, S.A.; Wols, B.A.; Yntema, D.R.; Lammertink, R.G.H. Photocatalytic Ceramic Membrane: Effect of the Illumination Intensity and Distribution. *J. Photochem. Photobiol. A Chem.* **2023**, *437*, 114469. [CrossRef]
37. Groeneveld, I.; Kanelli, M.; Ariese, F.; van Bommel, M.R. Parameters That Affect the Photodegradation of Dyes and Pigments in Solution and on Substrate—An Overview. *Dyes Pigments* **2023**, *210*, 110999. [CrossRef]
38. Saeed, M.; Muneer, M.; Haq, A.U.; Akram, N. Photocatalysis: An Effective Tool for Photodegradation of Dyes—A Review. *Environ. Sci. Pollut. Res.* **2021**, *29*, 293–311. [CrossRef]
39. Chiarello, L.M.; Mittersteiner, M.; de Jesus, P.C.; Andreaus, J.; Barcellos, I.O. Reuse of Enzymatically Treated Reactive Dyeing Baths: Evaluation of the Number of Reuse Cycles. *J. Clean. Prod.* **2020**, *267*, 122033. [CrossRef]
40. Nawaz, A.; Atif, M.; Khan, A.; Siddique, M.; Ali, N.; Naz, F.; Bilal, M.; Kim, T.H.; Momotko, M.; Haq, H.U.; et al. Solar Light Driven Degradation of Textile Dye Contaminants for Wastewater Treatment—Studies of Novel Polycationic Selenide Photocatalyst and Process Optimization by Response Surface Methodology Desirability Factor. *Chemosphere* **2023**, *328*, 138476. [CrossRef]
41. Javanbakht, V.; Mohammadian, M. Photo-Assisted Advanced Oxidation Processes for Efficient Removal of Anionic and Cationic Dyes Using Bentonite/TiO_2 Nano-Photocatalyst Immobilized with Silver Nanoparticles. *J. Mol. Struct.* **2021**, *1239*, 130496. [CrossRef]
42. Lin, Q.; Huang, X.; Lu, L.; Tang, D. Snowflake-like CdS@$ZnIn_2S_4$ Heterojunction-Based Photocatalyst-Electrolyte Effect: An Innovative Mode for Photoelectrochemical Immunoassay. *Biosens. Bioelectron.* **2022**, *216*, 114679. [CrossRef] [PubMed]
43. Uma, H.B.; Ananda, S.; Nandaprakash, M.B. High Efficient Photocatalytic Treatment of Textile Dye and Antibacterial Activity via Electrochemically Synthesized Ni-Doped ZnO Nano Photocatalysts. *Chem. Data Collect.* **2019**, *24*, 100301. [CrossRef]
44. Khandan Nasab, N.; Sabouri, Z.; Ghazal, S.; Darroudi, M. Green-Based Synthesis of Mixed-Phase Silver Nanoparticles as an Effective Photocatalyst and Investigation of Their Antibacterial Properties. *J. Mol. Struct.* **2020**, *1203*, 127411. [CrossRef]

45. Ahmed, A.; Usman, M.; Yu, B.; Ding, X.; Peng, Q.; Shen, Y.; Cong, H. Efficient Photocatalytic Degradation of Toxic Alizarin Yellow R Dye from Industrial Wastewater Using Biosynthesized Fe Nanoparticle and Study of Factors Affecting the Degradation Rate. *J. Photochem. Photobiol. B Biol.* **2020**, *202*, 111682. [CrossRef]
46. Zhao, J.; Wu, Q.X.; Cheng, X.D.; Su, T.; Wang, X.H.; Zhang, W.N.; Lu, Y.M.; Chen, Y. Biodegradation and Detoxification of the Triphenylmethane Dye Coomassie Brilliant Blue by the Extracellular Enzymes from Mycelia of Lactarius Deliciosus. *Front. Chem. Sci. Eng.* **2021**, *15*, 421–436. [CrossRef]
47. Bukallah, S.B.; Rauf, M.A.; Ashraf, S.S. Photocatalytic Decoloration of Coomassie Brilliant Blue with Titanium Oxide. *Dyes Pigments* **2007**, *72*, 353–356. [CrossRef]
48. Salem, M.S.; Wassel, A.R.; Fedawy, M.; Shaker, A.; Al-Bagawia, A.H.; Aleid, G.M.; El-Mahalawy, A.M. Integration of Biocompatible Coomassie Brilliant Blue Dye on Silicon in Organic/Inorganic Heterojunction for Photodetection Applications. *J. Phys. Chem. Solids* **2022**, *169*, 110890. [CrossRef]
49. Khataee, A.R.; Kasiri, M.B. Photocatalytic Degradation of Organic Dyes in the Presence of Nanostructured Titanium Dioxide: Influence of the Chemical Structure of Dyes. *J. Mol. Catal. A Chem.* **2010**, *328*, 8–26. [CrossRef]
50. Rayaroth, M.P.; Aravind, U.K.; Aravindakumar, C.T. Sonochemical Degradation of Coomassie Brilliant Blue: Effect of Frequency, Power Density, PH and Various Additives. *Chemosphere* **2015**, *119*, 848–855. [CrossRef]
51. Rayaroth, M.P.; Aravind, U.K.; Aravindakumar, C.T. Ultrasound Based AOP for Emerging Pollutants: From Degradation to Mechanism. *Environ. Sci. Pollut. Res.* **2017**, *24*, 6261–6269. [CrossRef] [PubMed]
52. Tian, J.; Cao, X.; Sun, T.; Miao, H.; Chen, Z.; Xue, W.; Fan, J.; Liu, E. Efficient Photocatalytic H2 Evolution over NiMoO4/Twinned-Cd0. 5Zn0. 5S Double S-Scheme Homo-Heterojunctions. *Compos. Part B Eng.* **2024**, *277*, 111389. [CrossRef]
53. Wang, Q.; Zhao, Y.; Zhang, Z.; Liao, S.; Deng, Y.; Wang, X.; Ye, Q.; Wang, K. Hydrothermal Preparation of Sn_3O_4/TiO_2 Nanotube Arrays as Effective Photocatalysts for Boosting Photocatalytic Dye Degradation and Hydrogen Production. *Ceram. Int.* **2023**, *49*, 5977–5985. [CrossRef]
54. Wang, Q.; Li, H.; Yu, X.; Jia, Y.; Chang, Y.; Gao, S. Morphology Regulated Bi_2WO_6 Nanoparticles on TiO_2 Nanotubes by Solvothermal Sb^{3+} Doping as Effective Photocatalysts for Wastewater Treatment. *Electrochim. Acta* **2020**, *330*, 135167. [CrossRef]